Computer Modeling in Engineering & Sciences CMES, vol.123, no.2, pp.717-737, 2020

Identification of the Discrete Element Model Parameters for Rock-Like Brittle Materials

Rui Chen[1, 2], Yong Wang[1, 2], Ruitao Peng[1, 2, *], Shengqiang Jiang[1, 2], Congfang Hu[1, 2] and Ziheng Zhao[1, 2]

Abstract: An inverse method for parameters identification of discrete element model combined with experiment is proposed. The inverse problem of parameter identification is transmitted to solve an optimization problem by minimizing the distance between the numerical calculations and experiment responses. In this method, the discrete element method is employed as numerical calculator for the forward problem. Then, the orthogonal experiment design with range analysis was used to carry out parameters sensitivity analysis. In addition, to improve the computational efficiency, the approximate model technique is used to replace the actual computational model. The intergeneration projection genetic algorithm (IP-GA) is employed as the optimization algorithm. Consequently, the parameters of the discrete element model are determined. To verify the effectiveness and accuracy of the inverse results, the comparisons of shape deviation experiments with discrete element simulations are provided. It indicates that the effective and reliable discrete element model parameters can be quickly obtained through several sets of experimental data. Hence, this inverse method can be applied more widely to determine the parameters of discrete element model for other materials.

Keywords: Discrete element model, parameter determination, rock-like materials, IP-GA, inverse method.

1 Introduction

In nature, rock is a geological material with discontinuities, heterogeneity, anisotropy and non-linearity. With the rapid development of rock engineering, such as tunnel construction for high-speed rail [Bandini, Berry, Cormio et al. (2017)], oil and shale gas exploitation [Hogan, Rogers, Spray et al. (2012)], radioactive waste storage

[1] School of Mechanical Engineering, Xiangtan University, Xiangtan, 411105, China.
[2] Engineering Research Center for Complex Track Processing Technology and Equipment, Xiangtan University, Xiangtan, 411105, China.
[*] Corresponding Author: Ruitao Peng. Email: pengruitao@xtu.edu.cn.
Received: 23 May 2019; Accepted: 10 March 2020.

[Vaissiere, Armand and Talandier (2015)], it is of great significance to investigate the mechanical characteristics and failure behaviors of rock materials when they are suffering from different loadings. Traditionally, experimental techniques are used to study mechanical properties of rock materials [Asprone, Cadoni, Prota et al. (2009); Zhang and Zhao (2014); Liu, Ji, Liu et al. (2017); Krasyuk, Lugin and Pavlov (2019)]. However, the laboratory experiments or tests are very time-consuming and expensive. Hence, numerical computation is widely adopted to study the mechanical behaviors of materials. Among these numerical methods, discrete element method (DEM) [Cundall and Strack (1979)] is an effective tool to investigate the mechanical properties of rock materials.

Compared with finite element method that is based on continuum mechanics, DEM takes into account most kinds of discontinuities and material breakage properties with multiple fractures. Over the past decades, many studies have used DEM to study the mechanical characteristics of rock-like materials [Su and Akcin (2011); Karampinos, Hadjigeorgiou, Hazzard et al. (2015); Lee, Moon and Haimson (2016); Yoon, Stephansson, Zang et al. (2017); Espada, Muralha, Lemos et al. (2018)]. These researches have indicated that the main advantage of DEM over other computational tools is its micromechanical representation of discontinuous media, which provided a better understanding of the step-path failure mechanism. Moreover, finite-discrete element method (FDEM) was proposed by take advantages of continuum and discontinuum techniques [Munjiza (2004); Munjiza, Knight and Rougier (2011, 2015)]. FDEM couples FEM and DEM through generating a finite element mesh separately for each discrete element located in the calculation domain, and has been successfully applied to simulate material failure and fracture problems in recent years [Munjiza, Andrews and White (1999); Munjiza, Bangash and John (2004); Mahabadi, Grasselli and Munjiza (2010); Lukas, D'Albano and Munjiza (2014)].

As using DEM for numerical computation, a set of model parameter values should be provided. The accuracy of numerical calculation depends on these appropriate parameters to some extent. Some model parameters can be obtained directly through experiments, while others should be determined by the indirect ways, as these parameters describe the mechanical behavior of materials at the micro level. Generally, these parameters can be obtained by calibration of macroscopic responses, in which the values are gradually adjusted till the error between experiment and numerical computation is very little. Trial and error method is usually carried out as a calibration of DEM parameters [Potyondy and Cundall (2004); Yang, Jiao and Lei (2006); Tan, Yang and Sheng (2008); Yang, Sheng, Ye et al. (2010); Jiang, Li, Zhang et al. (2018)]. However, the trial and error method for parameter identification depends on previous experience, and it has typical feature of randomness and blindness. Moreover, this method is very expensive and time consuming for performing DEM computation. To overcome these difficulties, it is obviously valuable to seek a reliable method to identify these model parameters. Among those proposed methods, the method by employing inverse techniques appears more promising.

Parameters identification by inverse technique is classified as an inverse problem, which consists of using the actual results of measurements to infer the values of the parameters that characterize the system [Tarantola (2005); Aster, Borchers and Thurber (2013)]. The inverse technique for determining model parameters mainly use optimization methods by minimizing the distance between numerical calculations and experiment responses. Many researchers have successfully used the inverse techniques to identify model parameters of different materials [Park and Park (2015); Benvenuti, Kloss and Pirker (2016); He, Xu, Peng et al. (2017); Bocciarelli and Ranzi (2018); Ren, Chen, Li et al. (2018); Zhang, Liu, Qiang et al. (2019)]. The inverse method used to determine DEM parameters adopts a complex relationship between the macroscopic response from experimental measurements and the microscopic input constants of the model. The relationship is usually represented by a known mathematical model, which defines the forward problem. Therefore, if a number of accurate experimental responses are available, the model parameters of DEM may be identified by solving an inverse problem properly formulated.

Therefore, in this paper, an inverse technique for identifying the model parameters of DEM is developed. The research ideas of this paper are as follows: firstly, in Section 2, the main ideas and solving steps of the inverse method are presented. In Section 3, the specific steps of the method are illustrated by introducing the forward calculation, sensitivity analysis, approximate model and optimization algorithm, in which an effective inverse technique to identify microscopic parameters of DEM model has been successfully achieved. In Section 4, the inverse results are provided and some important discussions on DEM computation for the shape deviation of specimen under the uniaxial compression are performed for verification of the inverse method.

2 Inverse problem description

The parameters identification problem for DEM model can be solved as an optimization problem, and the inverse analysis process for determination of parameters is shown in Fig. 1. First of all, material mechanics experiments should be performed to obtain the measured responses of material, which provide input data and validation data for parameters identification. Based on the mechanical experiment, the corresponding forward problem model by DEM is established. Secondly, in order to ensure a strong dependence between the input parameters and the output responses, sensitivity analysis for model parameters should be carried out. To enhance the computational efficiency, the approximate model is used instead of numerical calculations model. Then using the forward solver to obtain the calculation response, the inverse problem objective function is constructed according to the actual problem and numerical computation. The objective function is described to estimate the sum of square of deviations between numerical and experimental data. Objective function can be expressed as follows:

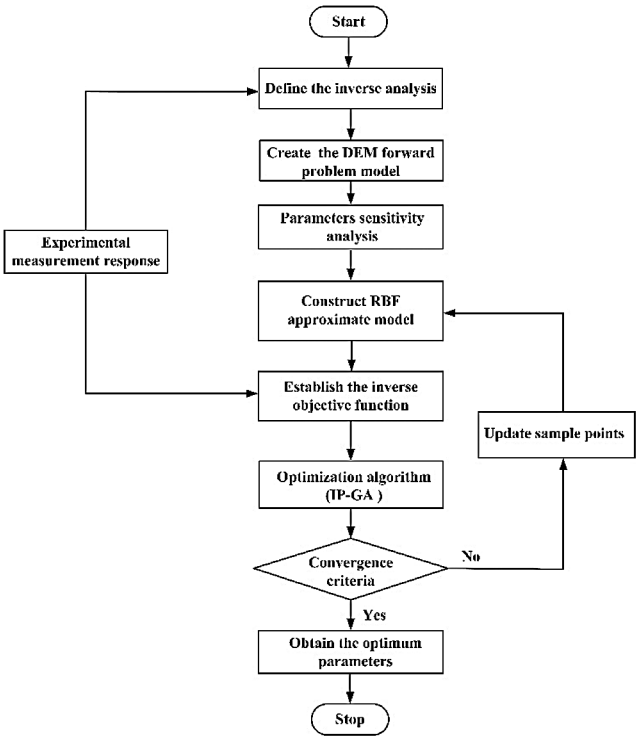

Figure 1: Schematic chart for the parameters identification process

$$F_{obj}(r) = \sum_{i=1}^{n} \left(y_i^m - y_i^c(r)\right)^2 \tag{1}$$

where r is a vector that represents the DEM inversed parameters, y_i^m is the response measured from experiment, $y_i^c(r)$ is the computational response obtained from the forward solver, and n is the number of samples.

Finally, an efficient and reliable optimization algorithm is adopted to obtain the inverse results. The convergence criterion is used to judge whether the identified parameter is available. If the convergence criterion is not satisfied, the new samples should be added to reconstruct approximation model and it should repeat these steps until it is satisfied.

3 Parameter identification process applied on the discrete element model

3.1 Discrete element method (DEM) and bonded particle model (BPM)

DEM is an effective numerical calculation method based on particle interactions [Cundall and Strack (1979)]. In the DEM, materials are treated as a collection of many discrete particles that are connected by bonds. Each particle is considered as a rigid entity with

defined surface and limited mass. The particle interaction is a dynamic process and the movement of particles meets Newton's second law and force-displacement law. The movement can be divided translation and rotation, which are expressed as:

The translation motion:

$$\boldsymbol{F} = \boldsymbol{m}(\ddot{\boldsymbol{u}} - \boldsymbol{g}) \tag{2}$$

The rotation motion:

$$\boldsymbol{M} = \boldsymbol{I}\dot{\omega} + \omega \times \boldsymbol{L} \tag{3}$$

where $\boldsymbol{F}$ is the resultant force acting on the particle, m is the mass of particle, $\boldsymbol{g}$ is the gravity acceleration, $\boldsymbol{u}$ is the displace of the center mass of particle, $\boldsymbol{M}$ is the resultant moment caused by contacts, $\boldsymbol{I}$ is the inertia tensor of particle, ω is the angular velocity and $\boldsymbol{L}$ is the angular momentum.

Potyondy et al. [Potyondy and Cundall (2004)] proposed bonded particle model to represent the mechanical behaviors of brittle materials. In the BPM, all particles are bonded together by contacts and can interact with each other at their contact points by following an internal algorithm. In this work, BPM is used for DEM simulation of mechanical behavior of limestone. There are two forms in the BPM: contact bond and parallel bond. Parallel bond is widely used for describing the mechanical property of brittle material, as it describes the transmitting both the moment and torque between the particles, and the shear and tension force between the particles, as shown in Fig. 2. Therefore, parallel bond is adopted in this study.

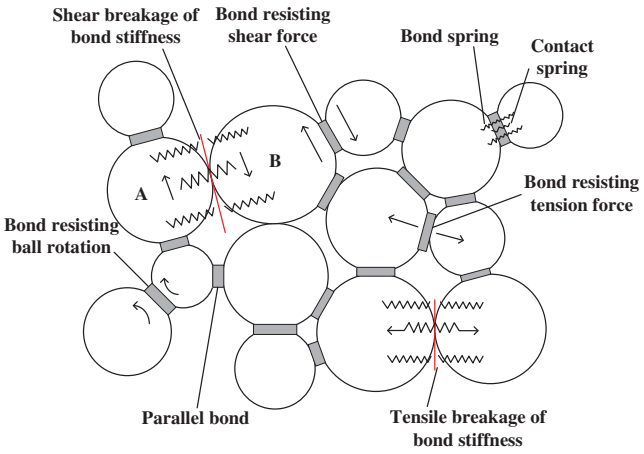

Figure 2: The BPM model diagram

The contact force between the particles can be divided into normal and shear components with respect to the contact plane as

$$F_i = F^n n_i + F^s t_i \tag{4}$$

where the contact force vector F_i represents the action of particle A on particle B. F^n and F^s denote the normal and shear force components, respectively. n_i and t_i are the normal and tangential unit vectors of the contact plane, respectively.

The magnitude of the tangential force F^s is computed in increments. As the two particles are in contact, F^s is initially zero, and then it is incremental with the corresponding tangential displacement increment. The normal force and the increment of shear force are calculated by

$$F^n = K^n U^n \tag{5}$$

$$\Delta F^s = -K^s \Delta U^s \tag{6}$$

where K^n and K^s are normal and shear stiffness values at the contact, respectively. U^n is the overlap of the two contacting particles, $\triangle F^s$ is the increment of the shear contact force, and $\triangle U^s$ is the relative shear displacement.

The maximum tensile and shear stresses acting on the bond periphery are computed (via beam theory) to be:

$$\sigma_{max} = \frac{-\bar{F}^n}{A} + \frac{|\bar{M}|}{I} R \tag{7}$$

$$\tau_{max} = \frac{\left|\bar{F}_i^s\right|}{A} \tag{8}$$

where A is the area of the cross section of a bond; I is the moment of inertia of the cross section of the bond; $\bar{F}$ and $\bar{M}$ denote the total force and moment associated with the parallel bond respectively; R is the radius of bond.

Once the tension or shear force exceeds the limit of normal strength or tangential strength between the particles ($\sigma_{max} \geq \sigma_{bond}$ *or* $\tau_{max} \geq \tau_{bond}$), the bond between the two particles can break. Simultaneously, the corresponding force and torque can be removed. The behaviors of the bond at contact are shown in Fig. 3.

There are eight microscopic parameters in the BPM: the friction coefficient of the particles μ, the radius multiplier of the parallel bond λ, the ball effective modulus E_c, the bond effective modulus $\overline{E_c}$, the normal-to-shear stiffness ratios of the ball K_n/K_s, the normal-to-shear stiffness ratios of the parallel bond $\overline{K_n}/\overline{K_s}$, the tensile strength of the parallel bond $\overline{\sigma_c}$, and the shear strength of the parallel bond $\overline{\tau_c}$. Some previous studies [Potyondy and Cundall (2004); Su and Akcin (2011)] indicated that for brittle materials, the radius multiplier of the parallel bond λ is set to be 1, the ball effective modulus E_c and the parallel bond effective modulus $\overline{E_c}$ are set to the same value, and the ball stiffness

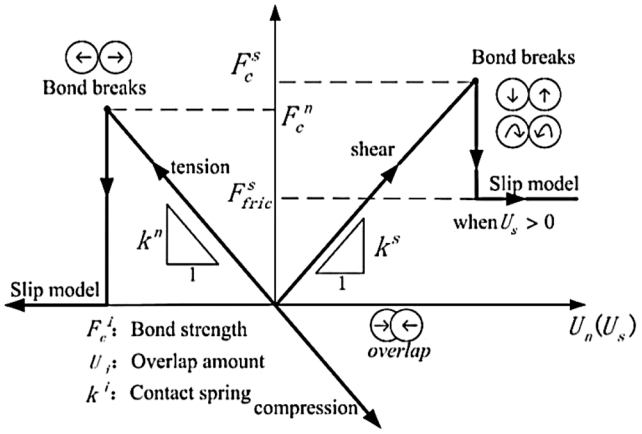

Figure 3: Behavior of the bond at contact in BPM

ratio K_n/K_s and the parallel bond stiffness ratio $\overline{K_n}/\overline{K_s}$ are set to the same value. Hence, there are other five parameters (μ, E_c, K_n/K_s, $\overline{\sigma_c}$ and $\overline{\tau_c}$), which are difficult to be determined directly by experiments. Therefore, an inverse technique is developed in this paper to identify these microscopic input parameters.

3.2 Forward analysis

In this study, a series of uniaxial compression experiments of limestone with different sample deviations from the reference Cvitanović et al. [Cvitanovic, Nikolic and Ibrahimbegovic (2015)] were applied to determine the parameters. As shown in Fig. 4, the group ID is the original control group. Group A and group D are used to test the effect of parallelism and verticality on the macroscopic properties, respectively. Based on

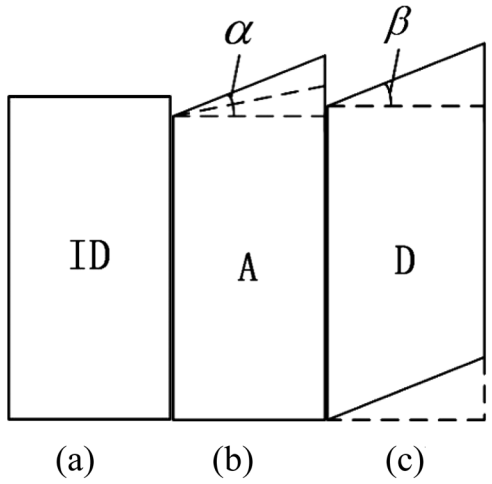

Figure 4: Basic groups of specimens-ID, A, D. (a) Original control group (b) Parallelism group and (c) Verticality group

these tests, the DEM model could be built. When the angle of parallelism deviation of specimen was 0° (Group ID), a corresponding DEM numerical model was established for forward computation. The top and bottom walls are set in the DEM model and made of horizontal straight lines to represent the upper and lower loading plates in compression test. The stiffness of walls is much bigger than the particle stiffness to avoid any distortion during testing, and the walls move toward the center of the model with a vertical velocity of 0.2 m/s to simulate the uniaxial compression process. Then, a two-dimensional DEM model for uniaxial compression test was constructed, as shown in Fig. 5. In this model, the length W, height L and density ρ were 53 mm, 126 mm and 2570 kg/m^3, respectively.

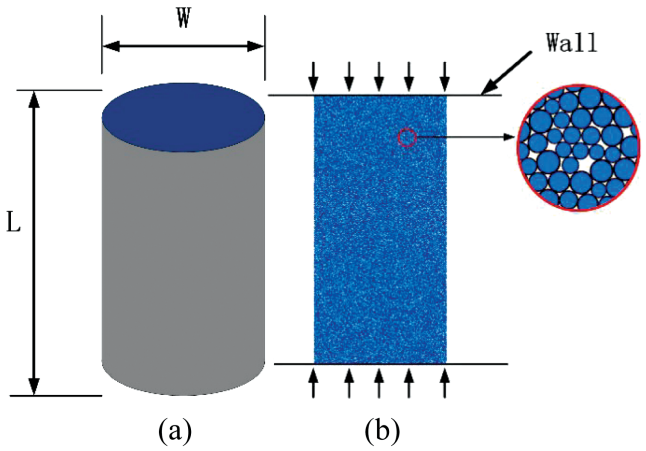

Figure 5: Specimen model and discrete element simulation model for group ID. (a) Specimen model (b) Discrete element model

Generally, the more the number of particles for constructing discrete element model is, the higher the accuracy of DEM model is. Several researchers have indicated that as the number of particles is more than 6000, the model could be accurate [Potyondy and Cundall (2004)]. In this study, three cases with different number of particles are discussed to investigate the effect of particle number. The computational results are shown in Fig. 6. It is found that the computational curves with different number of particle vary slightly and the computation time increases with the number of particle increases. Hence, in this work, to balance the accuracy and efficiency, the number of particle for DEM was 12,016, the maximum-to-minimum radius ratio was 1.66, and the minimum radius of particles was 0.3 mm.

3.3 Parameters sensitivity analysis

In the inverse technique for parameter identification, an essential condition is that the inversed parameters should be greatly sensitive to the measured responses for reducing the ill-posed problem [Aster, Borchers and Thurber (2013)]. Thus sensitivity analysis should be carried

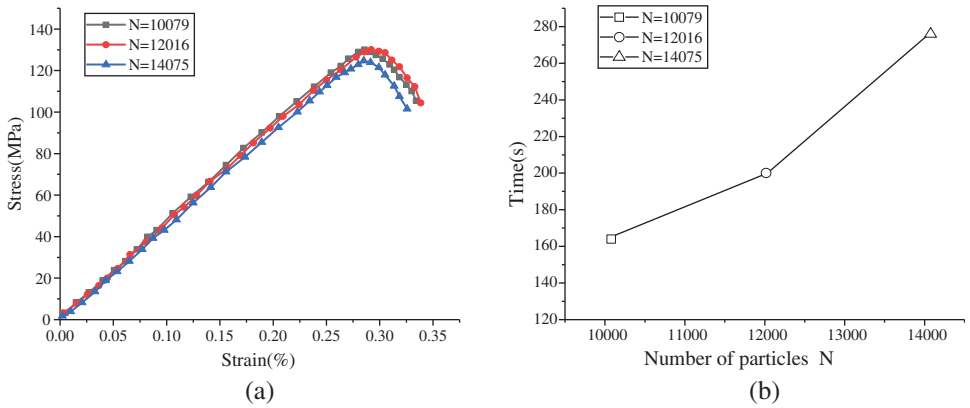

Figure 6: The DEM computation results under different particle number. (a) The stress-strain curves and (b) The computation time

out to study whether or not model parameters have a significant causal-effect on the responses. Then, these highly sensitive parameters are selected as inversed parameters.

The orthogonal experiment design (OED) method is an effective way to sensitivity analysis with multiple factors and multiple levels [Winer, Brown and Michels (1971)]. It is based on the orthogonality selected from comprehensive test of some representative points test, and these points have obvious features with uniformly dispersed, comparable and neat. Through OED and data analysis, it can obtain the relative importance and effect of model parameters to the responses. Then these five model parameters, μ, E_c, K_n/K_s, $\overline{\sigma_c}$ and $\overline{\tau_c}$, were selected as variables and a $L_{16}(4^5)$ orthogonal array was performed with factors and levels. In reference Potyondy et al. [Potyondy and Cundall (2004)], the values of these five parameters for rock materials have been obtained. Thus based on the previous study, in this work, the initial ranges of these five parameters for limestone can be given, $\mu[0.3, 0.6]$, $E_c[15\,GPa, 30\,GPa]$, $K_n/K_s[1.0, 3.0]$, $\overline{\sigma_c}[25\,MPa, 40\,MPa]$, and $\overline{\tau_c}[85\,MPa, 100\,MPa]$. As the level of these parameters is four, four values in each range have been taken uniformly. Hence, the levels of five parameters were [0.3, 0.4, 0.5, 0.6], [15 GPa, 20 GPa, 25 GPa, 30 GPa], [1.0, 1.67, 2.33, 3], [25 MPa, 30 MPa, 35 MPa, 40 MPa] and [85 MPa, 90 MPa, 95 MPa, 100 MPa], respectively. Through forward numerical computations, the three macroscopic response variables (Young's modulus E, Poisson's ratio υ, uniaxial compressive strength (UCS) σ_c) could be obtained with different sets of unknown parameters, as listed in Tab. 1.

According to the range analysis, the orthogonal experiment data of DEM computation was analyzed. It should be noted that K_i^x is the sum of the evaluation index of level i for factor x, $k_i^x = K_i^x/4$ and $R_x = max\{k_i^x\} - min\{k_i^x\}$. The greater the value of R is, the greater the impact of this factor on the result is. The analysis results were listed in Tab. 2.

From Tab. 2, it shows that the parameter E_c, K_n/K_s and $\overline{\sigma_c}$ have the greatest influence on E, υ and σ, respectively. And the corresponding R values are 28.89, 0.208 and 46.23,

Table 1: Results of orthogonal experiment

Number	Factors					Results		
	E_c (GPa)	k_n/k_s	$\overline{\sigma_c}$ (MPa)	$\overline{\tau_c}$ (MPa)	μ	E (GPa)	υ	σ_c (MPa)
1	15	1.0	25	85	0.3	31.95	0.134	104.62
2	15	1.67	30	90	0.4	29.04	0.224	112.96
3	15	2.33	35	95	0.5	27.44	0.275	121.97
4	15	3.0	40	100	0.6	26.26	0.313	123.85
5	20	1.0	30	95	0.6	44.38	0.096	136.49
6	20	1.67	25	100	0.5	39.41	0.21	98.15
7	20	2.33	40	85	0.4	36.16	0.285	135.39
8	20	3.0	35	90	0.3	33.96	0.338	110.49
9	25	1.0	35	100	0.4	54.05	0.121	145.06
10	25	1.67	40	95	0.3	47.68	0.239	145.25
11	25	2.33	25	90	0.6	46.46	0.267	93.99
12	25	3.0	30	85	0.5	43.44	0.318	100.03
13	30	1.0	40	90	0.5	65.55	0.108	161.38
14	30	1.67	35	85	0.6	59.41	0.202	141.13
15	30	2.33	30	100	0.3	53.51	0.298	105.02
16	30	3.0	25	95	0.4	51.75	0.323	84.2

respectively. In addition, in the range analysis of υ, μ has the second largest impact on υ. However, the R value of K_n/K_s is still more than 6 times the R value of μ. So the remaining two parameters μ and $\overline{\tau_c}$, they have little effect on the calculation results. Therefore, the three parameters (E_c, K_n/K_s and $\overline{\sigma_c}$) have greater sensitivity to the responses, which are defined as inversed parameters. According to the reference literatures [Potyondy and Cundall (2004); Yoon (2007); Zhang and Zhang (2017)], the values of parameter μ and $\overline{\tau_c}$ can be set to 0.5 and 90 MPa, respectively. Furthermore, it can be found from Tab. 1 that some computational responses are larger than the experimental responses, while some are smaller. Consequently, combined with the computational results of sensitivity analysis and experimental data, the range of the three inversed parameters could be initially obtained, as follows: E_c [20 GPa, 30 GPa], K_n/K_s [1, 3], and $\overline{\sigma_c}$ [30 MPa, 40 MPa].

3.4 Approximate model

Generally, thousands of forward computations may be performed in the process of parameters identification, which is time-consuming. In this study, it should take about

Table 2: Range analysis of Young's modulus, Poisson's ratio and UCS

Parameters	E_c	k_n/k_s	$\overline{\sigma_c}$	$\overline{\tau_c}$	μ
k_1 $(E/\upsilon/\sigma)$	28.67/0.237/ 115.85	48.98/0.115/ 136.89	42.39/0.234/ 95.24	42.74/0.235/ 120.29	41.78/0.252/ 116.35
k_2 $(E/\upsilon/\sigma)$	38.48/0.232/ 120.13	43.89/0.219/ 124.37	42.59/0.234/ 113.63	43.75/0.234/ 119.71	42.75/0.238/ 119.4
k_3 $(E/\upsilon/\sigma)$	47.91/0.236/ 121.08	40.89/0.281/ 114.09	43.72/0.234/ 129.66	42.81/0.233/ 121.98	43.96/0.228/ 120.38
k_4 $(E/\upsilon/\sigma)$	57.56/0.233/ 122.93	38.85/0.323/ 104.64	43.91/0.236/ 141.47	43.31/0.236/ 118.02	44.13/0.22/ 123.87
R_i $(E/\upsilon/\sigma)$	28.89/0.005/ 7.08	10.13/0.208/ 32.25	1.52/0.002/ 46.23	1.01/0.003/ 3.96	2.35/0.032/ 7.52

4 min of CPU times to perform single forward calculation by DEM. Therefore, the computational cost is unacceptable for parameter identification by inverse method. In order to improve the computational efficiency, in this work, the approximate model technique is adopted to replace the computational computation.

As constructing approximate model, it is necessary to provide enough samples. In this study, Latin hypercube design (LHD) method is used to generate samples as it is a space-filling design with constrainedly stratified sampling method [Peter and Bradley (2011)]. In this method, the sampling space are comprehensively stratified and split into a number of subintervals, and then random samples from each subinterval can be taken. It enables the sampling points to be distributed relatively uniformly in the whole design space, and divides uniformly the design space of each variable, and each variable has the same number of subintervals. As every level of each variable is uniformly used, the LHD method can reflect the characteristics of the whole design space with fewer sample points, which has the advantages of good balance and high efficiency.

In this study, 33 samples were produced by LHD method, as shown in Tab. 3. The approximate model technique with radical basis function (RBF) [Mysers and Montgomery (2002)], which is highly accurate for high-dimensional nonlinear problem, is used to construct the approximate model. The general form of RBF can be expressed as:

$$y(\mathbf{x}) = \sum_{i=1}^{m} w_i \varphi(\|\mathbf{x} - \mathbf{x}_i\|) \tag{9}$$

where $y(\mathbf{x})$ denotes the interpolation function, $\varphi(\|\mathbf{x} - \mathbf{x}_i\|)$ is radical basis function, $\|\mathbf{x} - \mathbf{x}_i\|$ is the distance between the vector $\mathbf{x}$ and $\mathbf{x}_i$, and w_i is the weight coefficient of each RBF, and m is the sum of basis functions. In this study, the Gaussian function is used as basis function, which is written as

Table 3: Samples generated by LHD method and the computational results

Number	Input			Output		
	E_c (GPa)	k_n/k_s	$\overline{\sigma_c}$ (MPa)	E (GPa)	v	σ_c (MPa)
1	20.03	2.89	38.15	35.05	0.312	119.84
2	26.00	2.82	34.12	45.77	0.308	112.87
3	29.18	2.69	30.82	51.85	0.300	108.24
4	27.86	1.47	32.43	56.16	0.186	128.77
5	21.51	2.19	31.16	39.85	0.263	113.76
6	23.74	1.02	32.67	51.76	0.111	139.78
7	25.23	1.92	34.59	48.07	0.239	127.98
8	29.41	1.59	35.63	58.25	0.202	138.4
9	21.18	1.36	34.96	43.35	0.171	141.17
10	28.99	1.44	39.31	58.62	0.183	154.38
11	27.61	1.84	35.20	53.04	0.230	132.21
12	24.09	1.22	39.52	50.47	0.149	155.35
13	21.84	2.22	36.21	40.35	0.266	129.25
14	24.95	1.98	39.75	47.19	0.245	142.98
15	25.55	2.49	31.79	46.11	0.286	113.35
16	20.80	2.57	37.41	37.31	0.292	129.42
17	26.94	2.34	33.02	49.22	0.275	119.08
18	22.09	1.08	36.68	47.47	0.124	147.87
19	24.59	1.18	37.94	51.94	0.142	151.99
20	26.03	1.63	30.62	51.28	0.207	120.54
21	22.58	2.03	32.10	42.49	0.249	118.02
22	23.08	2.43	31.64	41.87	0.282	113.27
23	27.27	1.74	36.49	52.99	0.220	136.89
24	22.90	2.78	38.82	40.41	0.306	124.68
25	28.64	2.65	33.38	51.02	0.297	117.16
26	29.81	2.99	38.51	51.83	0.318	123.63
27	28.11	2.07	37.20	52.68	0.253	135.62
28	23.48	1.69	30.11	45.91	0.214	115.51
29	26.52	1.30	35.75	54.81	0.162	147.23

Table 3 (continued).

Number	Input			Output		
	E_c (GPa)	k_n/k_s	$\overline{\sigma_c}$ (MPa)	E (GPa)	υ	σ_c (MPa)
30	20.45	2.29	33.83	37.52	0.271	120.07
31	25.10	2.61	34.10	44.63	0.295	115.17
32	25.48	2.70	34.38	45.18	0.302	115.09
33	26.12	1.86	35.88	49.72	0.234	131.46

$$\varphi = \exp(-\frac{\|\mathbf{x} - \mathbf{x}_i\|^2}{2\delta^2}) \tag{10}$$

where δ is the width of Gaussian function.

Then, in this work, the approximate model can be expressed as:

$$F(M) = y\left(E_c, \frac{k_n}{k_s}, \overline{\sigma_c}\right) \tag{11}$$

where M stands for 3 macroscopic responses, E, υ, and σ, respectively.

In this study, the front 30 samples were used to construct the RBF approximate model and the last three samples were used to verify the reliability of model. The simulation of the three samples and the RBF predicted output values (E, υ , σ_c) are shown in Tab. 4. It can be seen that the relative error between DEM calculation and prediction of RBF model was within 5%. Therefore, it indicated that this RBF approximation model is reliable.

Table 4: Comparison of simulation results with RBF verification results

Number	Simulation results			RBF verif results (Relative error)		
	E (GPa)	υ	σ_c (MPa)	E (GPa)	υ	σ_c (MPa)
1	44.63	0.295	115.17	44.84 (0.47%)	0.29 (-1.70%)	118.11 (2.55%)
2	45.18	0.302	115.09	45.23 (0.11%)	0.3 (-0.66%)	118.03 (2.55%)
3	49.72	0.234	131.46	50.07 (0.70%)	0.23 (-1.71%)	135.39 (2.99%)

3.5 IP-GA

In this study, intergeneration projection genetic algorithm (IP-GA) is adopted for optimization algorithm. In the IP-GA, the child generation is produced by using information from the parent and grandparent generations [Xu, Li and Wu (2001)]. IP-GA

is a modification based on micro GA (μGA), to make use of its feature of small population size per generation so as to maximize the efficiency. The intergeneration projection (IP) operator aims to find a better individual by jumping along the move direction of the best individuals at two consecutive generations so as to improve the convergence rate. The IP-GA combines the μGA with IP operator and whereby has a better global convergence performance. During this optimization algorithm, in this study, the number of binary bits of each parameter is taken as 8. Each generation is set to 5 individuals, the crossover probability is 0.9 and the stopping criterion is imposed to limit each IP-GA runs to a maximum of 300 generations.

4 Results and discussions

4.1 Results

Based on the above presented inverse method, the parameters of BPM for limestone are determined and the identified results are listed in Tab. 5. The convergence curves of IP-GA for determination of objective function are shown in Fig. 7(a). It can be seen that the IP-GA has good convergence performance. The convergence curve of IP-GA for the three inversion parameters is shown in Figs. 7(b)–7(d). It shows that the convergence efficiency is very good, and the maximum number of iterations is about 100.

Table 5: Inversed parameters and results

Inversed parameters	Search range	Inversed results
E_c	[20 GPa, 30 GPa]	27.01 GPa
K_n/K_s	[1, 3]	2.04
$\overline{\sigma_c}$	[30 MPa, 40 MPa]	35.55 MPa

As obtaining the identified result, the objective function value is just 0.0123, which satisfies the evaluation criteria. And the computational result compared with the experimental curve is shown in Fig. 8. In order to estimate the optimal fit between the calculated results and the experimental data, the results are evaluated using the relative error RE and the correlation coefficient CC. The functions of the expression are stated as follow:

$$RE = \frac{||y^C - y^M||}{||y^M||} \tag{12}$$

$$CC = \frac{\sum_{i=1}^{n} \left[y_i^C - \overline{X}(y^c)\right]\left[y_i^M - \overline{X}(y^M)\right]}{\left[y^C - \overline{X}(y^C)\right]\left[y^M - \overline{X}(y^M)\right]} \tag{13}$$

where n is the number of sampling points and $\overline{X}(\mathrm{y})$ is the average value of the responses. Generally, as the smaller the RE is and the closer the CC is to 1, it indicates that the compliance of the result is higher. Through the calculation, the *RE* is 0.0378 and the

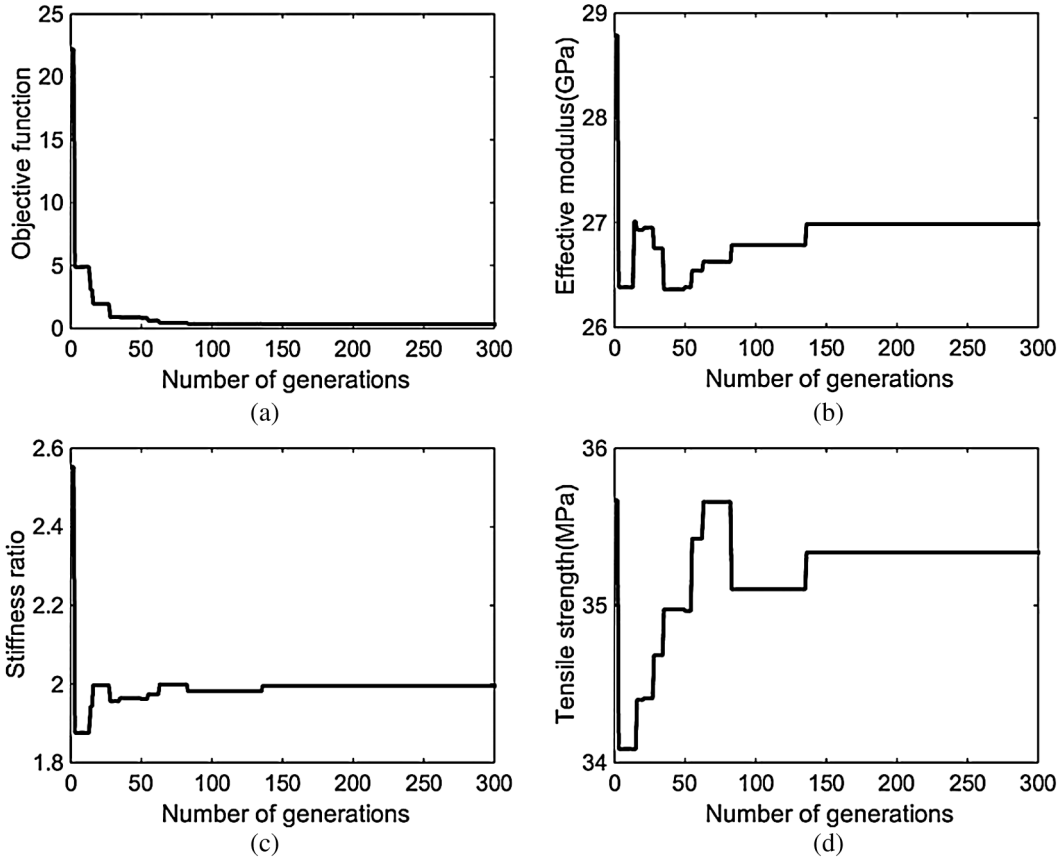

Figure 7: Convergence curves of parameter identification. (a) Objective function (b) Effective modulus (c) Stiffness ratio and (d) Tensile strength

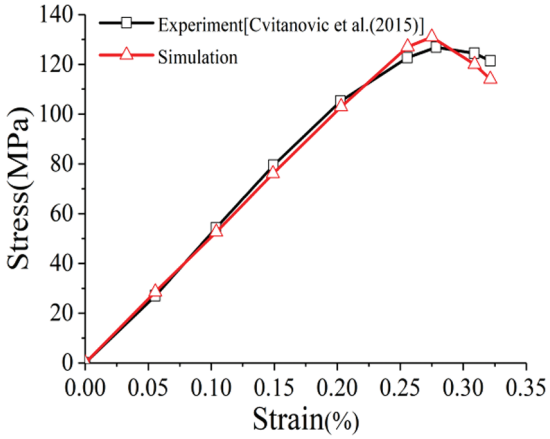

Figure 8: Comparison of experimental and simulation results

correlation coefficient *CC* is 0.997, which indicate that the numerical results based on the inverse parameter values are in good agreement with the experimental curves.

4.2 Discussions

In order to verify the availability and reliability of the inversed parameters, the numerical computations for the parallelism and verticality of the sample shape in uniaxial compression experiment were performed. According to the experiment of Cvitanović et al. [Cvitanovic, Nikolic and Ibrahimbegovic (2015)], different values of α and β (as shown in Fig. 4) were used to simulate by DEM. According to these experimental specimens, the corresponding DEM models were shown in Fig. 9.

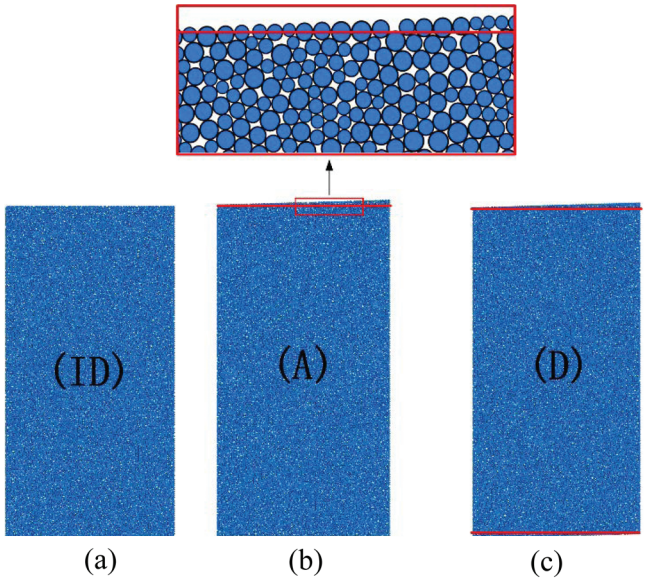

Figure 9: Discrete element model of specimens-ID, A, D. (a) Original control group (b) Parallelism group and (c) Verticality group

As shown in Fig. 10, it can be seen that the computational results were in good agreement with the experimental results under the four different shape deviations. Tab. 6 lists the evaluation indexes of the fitness of the two curves under each shape deviation. It is found that the values of *RE* are relatively little, the values of *CC* are close to 1. It is also noted that the minimum of *RE* is just 0.0452, while the maximum is 0.0886. And the minimum of *CC* is just 0.9804, while the maximum is 0.9972. Moreover, the *CC* for the response to the shape deviation of parallelism is slightly lower than the shape deviation of verticality, and the overall error is slightly greater than the vertical response. These results indicate that the parameters of DEM model identified by the developed inverse procedure in this study are available and reliable.

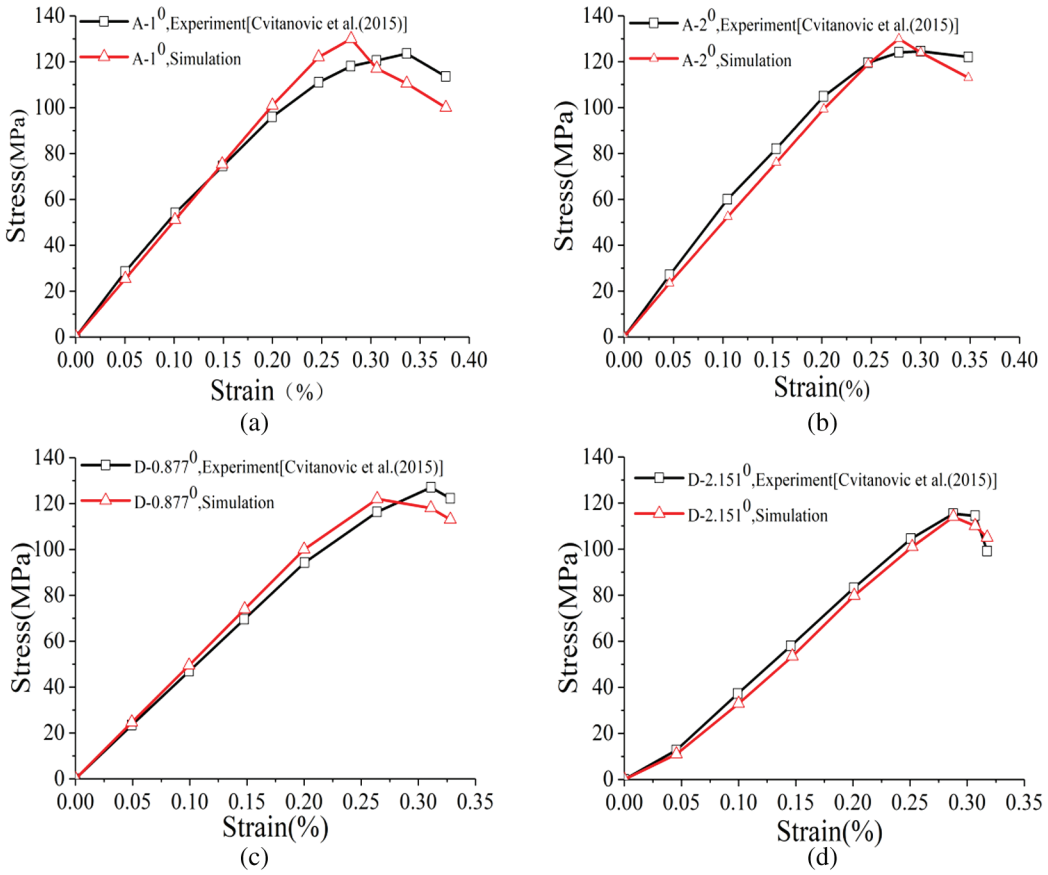

Figure 10: Comparison of experimental and simulation results. (a) α=1° (b) α=2° (c) β=0.877° and (d) β=2.151°

Table 6: Evaluation index of coincidence degree under different shape deviation

Shape deviation	RE	CC
Group A 1°	0.0886	0.9804
Group A 2°	0.0555	0.9951
Group D0.877°	0.0652	0.9923
Group D2.151°	0.0452	0.9972

5 Conclusions

In this study, an inverse method combined with experiment, numerical computation and optimization algorithm is developed to determine the microscopic parameters of DEM

model for limestone. To determinate the microscopic parameters, the sum of square of deviations between the experiment results and the calculated results has been minimized by the inverse method. A few experimental data, including the stress-strain curves, are used for evaluating the identified material parameters, and the calculated curves are in agreement with the experimental results well. Moreover, it verifies the accuracy of the inverse results with the shape deviation experiments and the results demonstrate the availability of this inverse method. Therefore, the developed inverse method is a helpful tool to efficiently and reliably identify model parameters, providing scientific basis for studying the mechanical properties of rock-like brittle materials.

Funding Statement: This work was supported by the National Natural Science Foundation of China (11602212) and the Natural Science Foundation of Hunan Province of China (2018JJ3509). This work was also supported by the National Natural Science Foundation of China (51605409, 11802258, 51775468).

Conflicts of Interest: The authors declare that they have no conflicts of interest to report regarding the present study.

References

Asprone, D.; Cadoni, E.; Prota, A.; Manfredi, G. (2009): Dynamic behavior of a Mediterranean an natural stone under tensile loading. *International Journal of Rock Mechanics and Mining Sciences*, vol. 46, no. 3, pp. 514-520. DOI 10.1016/j.ijrmms.2008.09.010.

Aster, R.; Borchers, B.; Thurber, C. (2013): *Parameter Estimation and Inverse Problems*. 2nd edition, New York: Elsevier.

Bandini, A.; Berry, P.; Cormio, C.; Colaiori, M.; Lisardi, A. (2017): Safe excavation of large section tunnels with Earth pressure balance tunnel boring machine in gassy rock masses: the Sparvo tunnel case study. *Tunnelling and Underground Space Technology*, vol. 67, pp. 85-97. DOI 10.1016/j.tust.2017.05.001.

Benvenuti, L.; Kloss, C.; Pirker, S. (2016): Identification of DEM simulation parameters by artificial neural networks and bulk experiments. *Powder Technology*, vol. 291, pp. 456-465. DOI 10.1016/j.powtec.2016.01.003.

Bocciarelli, M.; Ranzi, G. (2018): An inverse analysis approach for the identification of the hygro-thermo-chemical model parameters of concrete. *International Journal of Mechanical Sciences*, vol. 138-139, pp. 368-382. DOI 10.1016/j.ijmecsci.2018.01.035.

Cundall, P. A.; Strack, O. D. L. (1979): A discrete numerical model for granular assemblies. *Geotechnique*, vol. 29, no. 1, pp. 47-65. DOI 10.1680/geot.1979.29.1.47.

Cvitanovic, N. S.; Nikolic, M.; Ibrahimbegovic, A. (2015): Influence of specimen shape deviations on uniaxial compressive strength of limestone and similar rocks. *International Journal of Rock Mechanics and Mining Sciences*, vol. 80, pp. 357-372. DOI 10.1016/j.ijrmms.2015.10.008.

Espada, M.; Muralha, J.; Lemos, J. V.; Jiang, Q.; Feng, X. T. et al. (2018): Safety analysis of the left bank excavation slopes of Baihetan arch dam foundation using a discrete element model. *Rock Mechanics and Rock Engineering*, vol. 51, no. 8, pp. 2597-2615.

He, X.; Xu, C.; Peng, K.; Huang, G. (2017): Simultaneous identification of rock strength and fracture properties via scratch test. *Rock Mechanics and Rock Engineering*, vol. 50, no. 8, pp. 2227-2234. DOI 10.1007/s00603-017-1224-0.

Hogan, J. D.; Rogers, R. J.; Spray, J. G.; Boonsue, S. (2012): Dynamic fragmentation of granite for impact energies of 6-28. *Engineering Fracture Mechanics*, vol. 79, pp. 103-125. DOI 10.1016/j.engfracmech.2011.10.006.

Jiang, S.; Li, X.; Zhang, L.; Tan, Y.; Peng, R. et al. (2018): Discrete element simulation of SiC ceramic containing a single pre-existing flaw under uniaxial compression. *Ceramics International*, vol. 44, no. 3, pp. 3261-3276. DOI 10.1016/j.ceramint.2017.11.099.

Karampinos, E.; Hadjigeorgiou, J.; Hazzard, J.; Turcotte, P. (2015): Discrete element modelling of the buckling phenomenon in deep hard rock mines. *International Journal of Rock Mechanics and Mining Sciences*, vol. 80, pp. 346-356. DOI 10.1016/j.ijrmms.2015.10.007.

Krasyuk, A. M.; Lugin, I. V.; Pavlov, S. A. (2019): Experimental research into air distribution in a terminal subway station. *Tunnelling and Underground Space Technology*, vol. 85, pp. 21-28. DOI 10.1016/j.tust.2018.11.049.

Lee, H.; Moon, T.; Haimson, B. C. (2016): Borehole breakouts induced in arkosic sandstones and a discrete element analysis. *Rock Mechanics and Rock Engineering*, vol. 49, no. 4, pp. 1369-1388. DOI 10.1007/s00603-015-0812-0.

Liu, S.; Ji, H.; Liu, X.; Jiang, H. (2017): Experimental research on wear of conical pick interacting with coal-rock. *Engineering Failure Analysis*, vol. 74, pp. 172-187. DOI 10.1016/j.engfailanal.2017.01.013.

Lukas, T.; D'Albano, G. G. S.; Munjiza, A. (2014): Space decomposition based parallelization solutions for the combined finite-discrete element method in 2D. *Journal of Rock Mechanics and Geotechnical Engineering*, vol. 6, no. 6, pp. 607-615. DOI 10.1016/j.jrmge.2014.10.001.

Mahabadi, O. K.; Grasselli, G.; Munjiza, A. (2010): Y-GUI: a graphical user interface and pre-processor for the combined finite-discrete element code, Y2D, incorporating material heterogeneity. *Computers & Geosciences*, vol. 36, no. 2, pp. 241-252. DOI 10.1016/j.cageo.2009.05.010.

Munjiza, A. (2004): *The Combined Finite-Discrete Element Method*. Chichester, UK: John Wiley & Sons, Inc.

Munjiza, A.; Andrews, K. R. F.; White, J. K. (1999): Combined single and smeared crack model in combined finite-discrete element analysis. *International Journal for Numerical Methods in Engineering*, vol. 44, no. 1, pp. 41-57.

Munjiza, A.; Bangash, T.; John, N. W. M. (2004): The combined finite-discrete element method for structural failure and collapse. *Engineering Fracture Mechanics*, vol. 71, no. 4-6, pp. 469-483. DOI 10.1016/S0013-7944(03)00044-4.

Munjiza, A.; Knight, E. E.; Rougier, E. (2011): *Computational Mechanics of Discontinua*. Chichester, UK: John Wiley & Sons, Inc.

Munjiza, A.; Knight, E. E.; Rougier, E. (2015): *Large Strain Finite Element Method: A Practical Course*. Chichester, UK: John Wiley & Sons, Inc.

Mysers, R. H.; Montgomery, D. C. (2002): *Response Surface Methodology: Process and Product Optimization Using Designed Experiments*. New York: Wiley.

Park, D.; Park, E. S. (2015): Inverse parameter fitting of tunnels using a response surface approach. *International Journal of Rock Mechanics and Mining Sciences*, vol. 100, no. 77, pp. 11-18. DOI 10.1016/j.ijrmms.2015.03.026.

Peter, G.; Bradley, J. (2011): *Optimal Design of Experiments: A Case Study Approach*. New York: Wiley.

Potyondy, D. O.; Cundall, P. A. (2004): A bonded-particle model for rock. *International Journal of Rock Mechanics and Mining Sciences*, vol. 41, no. 8, pp. 1329-1364. DOI 10.1016/j.ijrmms.2004.09.011.

Ren, S.; Chen, G.; Li, T.; Chen, Q.; Li, S. (2018): A deep learning-based computational algorithm for identifying damage load condition: an artificial intelligence inverse problem solution for failure analysis. *Computer Modeling in Engineering & Sciences*, vol. 117, no. 3, pp. 287-307. DOI 10.31614/cmes.2018.04697.

Su, O.; Akcin, N. A. (2011): Numerical simulation of rock cutting using the discrete element method. *International Journal of Rock Mechanics and Mining Sciences*, vol. 48, no. 3, pp. 434-442. DOI 10.1016/j.ijrmms.2010.08.012.

Tan, Y.; Yang, D.; Sheng, Y. (2008): Study of polycrystalline Al_2O_3 machining cracks using discrete element method. *International Journal of Machine Tools and Manufacture*, vol. 48, no. 9, pp. 975-982. DOI 10.1016/j.ijmachtools.2008.01.010.

Tarantola, A. (2005). *Inverse Problem Theory and Methods for Model Parameter Estimation*. Philadelphia: Society for Industrial and Applied Mathematics.

Vaissiere, R.; Armand, G.; Talandier, J. (2015): Gas and water flow in an excavation-induced fracture network around an underground drift: a case study for a radioactive waste repository in clay rock. *Journal of Hydrology*, vol. 521, pp. 141-156. DOI 10.1016/j.jhydrol.2014.11.067.

Winer, B. J.; Brown, D. R.; Michels, K. M. (1971): *Statistical Principles in Experimental Design*. New York: McGraw-Hill.

Xu, Y. G.; Li, G. R.; Wu, Z. P. (2001): A novel hybrid genetic algorithm using local optimizer based on heuristic pattern move. *Applied Artificial Intelligence*, vol. 15, no. 7, pp. 601-631. DOI 10.1080/088395101750363966.

Yang, B. D.; Jiao, Y.; Lei, S. T. (2006): A study on the effects of micro-parameters on macro-properties for specimens created by bonded particles. *Engineering Computations*, vol. 23, no. 6, pp. 607-631. DOI 10.1108/02644400610680333.

Yang, D.; Sheng, Y.; Ye, J.; Tan, Y. (2010): Discrete element modeling of the microbond test of fiber reinforced composite. *Computational Materials Science*, vol. 49, no. 2, pp. 253-259. DOI 10.1016/j.commatsci.2010.05.003.

Yoon, J. (2007): Application of experimental design and optimization to PFC model calibration in uniaxial compression simulation. *International Journal of Rock Mechanics and Mining Sciences*, vol. 44, no. 6, pp. 871-889. DOI 10.1016/j.ijrmms.2007.01.004.

Yoon, J. S.; Stephansson, O.; Zang, A.; Min, K. B.; Lanaroc, F. (2017): Discrete bonded particle modelling of fault activation near a nuclear waste repository site and comparison to static rupture earthquake scaling laws. *International Journal of Rock Mechanics and Mining Sciences*, vol. 98, pp. 1-9. DOI 10.1016/j.ijrmms.2017.07.008.

Zhang, S.; Liu, H.; Qiang, J.; Gao, H.; Galar, D. et al. (2019): Optimization of well position and sampling frequency for groundwater monitoring and inverse identification of contamination source conditions using Bayes' theorem. *Computer Modeling in Engineering & Sciences*, vol. 119, no. 2, pp. 373-394. DOI 10.32604/cmes.2019.03825.

Zhang, Q.; Zhang, X. P. (2017): A numerical study on cracking processes in limestone by the *b*-value analysis of acoustic emissions. *Computers and Geotechnics*, vol. 92, pp. 1-10. DOI 10.1016/j.compgeo.2017.07.013.

Zhang, Q. B.; Zhao, J. (2014): A review of dynamic experimental techniques and mechanical behaviour of rock materials. *Rock Mechanics and Rock Engineering*, vol. 47, no. 4, pp. 1411-1478. DOI 10.1007/s00603-013-0463-y.